Journal Pre-proofs

Full recycling of spent lithium ion batteries with production of core-shell nanowires//exfoliated graphite asymmetric supercapacitor

Pier Giorgio Schiavi, Pietro Altimari, Robertino Zanoni, Francesca Pagnanelli

PII: S2095-4956(20)30715-4
DOI: https://doi.org/10.1016/j.jechem.2020.10.025
Reference: JECHEM 1650

To appear in: *Journal of Energy Chemistry*

Received Date: 31 August 2020
Revised Date: 12 October 2020
Accepted Date: 18 October 2020

Please cite this article as: P. Giorgio Schiavi, P. Altimari, R. Zanoni, F. Pagnanelli, Full recycling of spent lithium ion batteries with production of core-shell nanowires//exfoliated graphite asymmetric supercapacitor, *Journal of Energy Chemistry* (2020), doi: https://doi.org/10.1016/j.jechem.2020.10.025

Full recycling of spent lithium ion batteries with production of core-shell nanowires//exfoliated graphite asymmetric supercapacitor

Pier Giorgio Schiavi*, Pietro Altimari, Robertino Zanoni, Francesca Pagnanelli

Department of Chemistry, Sapienza University of Rome, Piazzale Aldo Moro n.5, 00185, Rome, Italy

*Corresponding author. E-mail address: piergiorgio.schiavi@uniroma1.it

Abstract

A novel process is reported which produces an asymmetric supercapacitor through the complete recycling of end-of-life lithium ion batteries. The electrodic powder recovered by industrial scale mechanical treatment of spent batteries was leached and the dissolved metals were precipitated as mixed metals carbonates. Nanowires battery-type positive electrodes were produced by electrodeposition into nanoporous alumina templates from the electrolytic baths prepared by dissolution of the precipitated carbonates. The impact of the different metals contained in the electrodic powder was evaluated by benchmarking the electrochemical performances of the recovered nanowires-based electrodes against electrodes produced by using high-purity salts. Presence of inactive Cu in the nanowires lowered the final capacitance of the electrodes while Ni showed a synergistic effect with cobalt providing a higher capacitance with respect to synthetic Co electrodes. The carbonaceous solid recovered after leaching was in-depth characterized and tested as negative electrode. Both the chemical and electrochemical characterization indicate that the recovered graphite is characterized by the presence of oxygen functionalities introduced by the leaching treatment. This has led to the obtainment of a recovered graphite characterized by an XPS C/O ratio, Raman spectrum and morphology close to literature reports for reduced graphene oxide. The asymmetric supercapacitor assembled using the recovered nanowires-based positive electrodes and graphite as negative electrodes has shown a specific capacitance of 42 Fg^{-1}, computed including the whole weight of the positive electrode and recovered graphite, providing a maximum energy density of ~9 $Whkg^{-1}$ and a power density of 416 Wkg^{-1} at 2.5 mA cm^{-2}.

Keywords: Lithium ion battery recyling; Core-shell nanowires; Supercapacitors; Closed-loop recycling process

1. Introduction

The application of Li-ion batteries (LIBs) has been steadily increasing over the past decades, driven by the growing market of consumer electronics. A further growth in the LIBs market has been recently observed, stimulated by the increasing diffusion of electric vehicles and by the need for storing the energy produced from discontinuous renewable sources [1]. Accordingly, a huge amount of end-of-life LIBs will be disposed in the next years, and efficient processes for LIBs recycling become fundamental in view of the potential threat to environmental and human safety represented by exhaust electrode materials. Furthermore, LIBs electrodic materials include strategic or critical raw materials such as graphite, cobalt and nickel that can be reintroduced in the energy storage devices manufacturing chain. The major obstacles encountered with the extensive LIBs recycling processes are their high cost and negative environmental impact. LIBs recycling is currently carried out using pyrometallurgical processes, but electrodic materials such as lithium, aluminium and graphite are involved in secondary reactions or lost in the smelting slag [2]. On the other hand, while hydrometallurgical processes have lower costs and emissions than pyrometallurgical ones, the associated complex chemistry of the electrodic materials makes it challenging the separation of the various materials. Hydrometallurgical processes can be implemented ensuring a complete recovery of all components of the different electrodic materials into high purity separate streams (Co, Ni, salts) [3]. A major bottleneck hindering the economic and environmental sustainability of hydrometallurgical processes is represented by the numerous and costly operations performed to separate the different electrode materials in order to obtain high purity Co, Ni products. Cobalt and nickel exhibit similar physicochemical properties and can be separated only by lengthy and complex separation-purification stages, including leaching, precipitations, solvent extractions, stripping, electrowinning. These processes imply a large consumption of reagents and the generation of large waste volumes which may hinder economic and environmentally sustainable hydrometallurgical recycling processes [2].

A promising strategy to overcome these issues is the integration of hydrometallurgical processes with the production of new high-performance materials to be applied in the energy storage devices production, excluding the costly and complex separation of the different metals. Several groups have developed hydrometallurgical processes for the re-synthesis of new active materials based on mixed oxides ($Li_aNi_bMn_cCo_dO_2$, $a+b+c+d=2$) and hydroxides starting from end-of-life LIBs, thus avoiding the separation of metals [4–6]. Scarce attention is generally paid to the valorisation of the carbonaceous solid [7,8] resulting

after the metals extraction during the hydrometallurgical LIBs recycling, including its reuse and in-depth characterization [9–11]. Just some research groups have recently begun examining possible strategies for the reuse of graphite for energy storage applications [12–14]. In addition, the production of new energy storage materials from recycled LIBs should also take into account the continuous boost for the development of advanced high-performance energy storage devices. In this perspective, and considering the low power density of LIBs, many efforts are currently devoted to the study of new high-performance energy storage devices. Electrochemical capacitors have attracted considerable attention due to their high-power density, long life cycling stability and fast energy delivery [15]. Nevertheless, electrochemical capacitors exhibit very low energy density, especially if compared with batteries [16,17]. In order to overcome this limitation, researchers have recently focused on the development of asymmetric supercapacitors, which are composed of a battery-type electrode and capacitive-type electrode. Capacitive-type electrodes store energy by charge separation at the double layer at the electrode/solution interface. These electrodes are typically composed by high surface area carbonaceous materials to ensure satisfactory electric conductivity and high specific capacity [18,19]. Battery-type electrodes are composed of pseudocapacitive materials that ensure the energy storage by fast reversible redox reactions. Although noble metal oxides (RuO_2 and IrO_2) are known as the most effective pseudocapacitive electrode materials, due to their high cost [20–22] the attention is currently focused on pseudocapacitive materials based on transition metals oxides/ hydroxides (Co, Ni, Mn, Fe) [23–25]. Despite their high delivered capacitance, pseudocapacitive materials suffer from their poor conductivity that limits the rate performance and the life-span of the final devices [26]. To improve the electrode conductivity, generally the electroactive pseudocapacitive materials are coupled with high conductivity materials, such as carbon materials or metallic foams, requiring the employment of insulating binder to ensure contact between the high conductivity materials and the active phase [27–32]. A different approach to ensure high conductivity of the electrodes involves the hydrothermal synthesis route. Here, metal oxide/hydroxide nanowires with a metallic core are attained by costly controlled thermal reduction and oxidation stages [33]. Further, the hydrothermal synthesis route does not effectively allow to control the nanowire aspect ratio and length. Alternatively, metallic nanowires with controlled aspect ratio and length can be directly produced by template electrodeposition [34,35].

In this work, a novel process allowing for the full recycling of the electrodic materials (both metals and graphite) of end of life LIBs by the direct production of an asymmetric supercapacitor is proposed. In order to

evaluate the potential scale-up of the proposed process, the electrodic powder recovered by industrial scale crushing and sieving of spent LIBs was used. A positive battery-type electrode was produced by an adapted electrodeposition method previously developed by the authors to synthesize nanowires electrodes [34,35]. With this method, an array of metal nanowires standing over a thin current collector plate can be produced by electrodeposition into the nanopores of anodized alumina templates and successive selective dissolution of alumina. The implementation of this strategy allows controlling the nanowires length distribution and can ensure the direct formation of a metallic core covered by a thin metal oxide/hydroxide layer. This can enhance the electronic conductivity and prevent the application of conductive binders. The impact of impurities (Cu, Fe, Al) contained in the electrodic powder was evaluated by benchmarking the electrochemical performances of the recovered nanowires-based electrodes against electrodes produced by using high-purity salts. Such impurities have been generally excluded by many studies through the manual dismantling and separation of the electrodic powder [36,37]. Along with the direct synthesis of metal nanowire electrodes, the graphite fraction from the electrode powder was recovered and characterized to evaluate its potential reuse as negative electrode material. In accordance with this idea and to definitively assess the effectiveness of the proposed recycling process, a supercapacitor cell was assembled by simultaneously employing the recovered graphite and the synthesized metal nanowire electrode as positive and negative electrode materials, respectively.

2. Experimental

2.1 Recylcing process

The implemented recycling process was adapted from our recently published work [34]. The overall scheme of process is reported in Fig. 1. Briefly, exhausted LIBs were collected, crushed and sieved by an Italian waste disposal company (SEVal s.r.l.). Following crushing, a sample of 50 kg was sieved by using a vibrating sieve with a grid's mesh size of 0.5 mm, which allowed separating the electrodic powder. Metal extraction was performed by leaching 200 g of electrodic powder using sulphuric acid and hydrogen peroxide allowing attaining a metals extraction yield up to 96% [38]. Following leaching, a filtration was performed to separate the residual carbon fraction. The carbon fraction, mainly composed of graphite, was treated by a subsequent acid leaching in order to eliminate all the metal impurities. The graphite recovered after the second leaching was employed as negative electrode in the asymmetric supercapacitor. The metals content in the recovered graphite was estimated by atomic absorption spectroscopy (AAS - Analytic Jena ContrAA300) after microwave

assisted leaching (Milestone Ethos Microwave Digestion System) of the samples. The extracted metals (Co, Ni, Mn, Cu, Cd, Al) resulting from the first leachate were recovered by following two different precipitation routes, both including a preliminary stage (purification) to selectively precipitate metal impurities (Cu, Fe, Al), followed by a second stage to precipitate target metals (Co, Ni). The two precipitation routes differed from each other for the pH of the preliminary purification performed to remove Cu, Fe, and Al impurities. This purification was carried out at pH 4 and 6 in the two routes, respectively. After filtration of the precipitated metal impurities, with both the routes, Na_2CO_3 was added to the solutions until reaching pH 8. The precipitated cobalt-rich carbonates were filtered and washed until the Na^+ concentration in the washing solution was lower than 10 mgL^{-1}. The electrolytic baths were then obtained by dissolving the carbonates in the smallest amount of H_2SO_4 and adding 1 mL of H_2O_2. These concentrated solutions were diluted to a volume of 50 mL with distilled water and 50 gL^{-1} of H_3BO_3 were added to any electrolytic bath. The content of any metal in the electrolytic solutions was measured by AAS.

2.2 Synthesis of nanowires-based electrodes

The positive electrodes of the asymmetric supercapacitors were synthesized by a template electrodeposition method [34,35]. Nanowires were synthesized by electrodeposition into the nanopores of an alumina template generated by a one-step anodization of low-purity aluminium. Electrodeposition was performed in a magnetically stirred three-electrode jacketed glass cell at constant temperature of 35 ± 0.2 °C. A 25x20 mm Pt gauze, Ag/AgCl saturated electrode and anodic alumina with exposed area of 1.3 cm^2 were used as counter, reference and working electrode, respectively. The electrolytes employed to perform the electrodeposition were obtained by dissolving the two metals carbonates as above descripted. The electrodes produced from the carbonates purified at pH 4 and pH 6 will be denoted throughout the article as Rec-4 and Rec-6 electrodes. The electrodeposition was performed by applying a constant voltage signal of −8 V vs Ag/AgCl for 100 ms and then the current was kept at zero for 2000 ms. These two pulses were looped until the alumina nanopores was filled. After this electrodeposition stage, the filled alumina template undergone a subsequent cobalt electrodeposition for the current collector generation. This electrodeposition was carried out until a charge of 60 C was transferred and a thin cobalt film above the alumina template was formed. To produce electrodes current collector the same conditions for the nanowires electrodeposition were employed but using a bath composed of 300 gL^{-1} $CoSO_4$ $7H_2O$. Finally, the electrodes were obtained after alumina and aluminium removal by selective etching in NaOH 6 M. In order to evaluate the role of the metal impurities, the same synthesis

procedure was replicated employing synthetic solutions for the production of a cobalt nanowires-based electrode (Co-NW). Further, the role of copper impurity was evaluated by the production of a synthetic cobalt-copper nanowire-based electrode (CoCu-NW).

2.3 Electrochemical measurements

Nanowires-based electrodes and graphite were tested respectively as positive and negative electrodes. The electrochemical behaviour of the electrodes was studied by cyclic voltammetry (CV) and galvanostatic cycling (GC) experiments. All the experiments were carried out using three-electrode jacketed glass cell at constant temperature of 25°C. Ag/AgCl, platinum spiral and the electrode under study with an exposed area of 0.5 cm2 were the reference, counter and working electrode, respectively. KOH 1 M was the electrolyte solutions. CV were performed at different scan rates of 10, 20, 50, 100, 200 mVs^{-1}. For the nanowires-based electrodes, CV and GC were carried out within a potential range of -0.2 - 0.5 V and GC were performed at constant current densities of 2, 4, 8, 12, 15, 20 mA cm^{-2}. These CV and GC electrochemical experiments were triplicated using three new electrodes. GC of graphite electrodes were performed at the current densities of 1, 2, 5, 10 A g^{-1} in a potential range within -1.1 and 0 V. The supercapacitors were assembled in a Swagelock T-cell. Two Whatman glass fibre membranes were used to separate the positive and the negative electrodes and KOH 1 M was the electrolyte solutions (Fig.S4). Negative electrodes were prepared by casting a dispersion of the recovered graphite on a titanium foil current collector. The dispersion was composed of 10% of PVDF binder and 90% of recovered graphite in 2-propanol.

2.4 Electrodes characterizations

Field emission scanning electron microscopy (SEM, Zeiss Auriga) was employed to characterize the morphology and size of electrodes. Powder X-ray diffraction (XRD, Rigaku, D-Max Ultima) employing Cu Kα radiation was used to identify the crystalline phase of the recovered graphite. X-ray photoelectron spectra were acquired using a modified Omicron NanoTechnology MXPS system. The spectra were excited by achromatic Al Ka and Mg Ka photons ($h\nu$= 1486.6 and 1253.6 eV, respectively), generated operating the anode at 14 kV, 14 mA. Experimental spectra were theoretically reconstructed by fitting the peaks to symmetric Voigt functions and the background to a Shirley or a linear function. XPS atomic ratios (±10% associated error) were obtained from experimentally determined area ratios, corrected for the corresponding theoretical cross sections and for a square root dependence of the photoelectrons kinetic energies. All the samples were mounted on small

amagnetic stainless steel tips with a conductive adhesive tape, which only exposed the sample to radiation. Peak assignments were given by reference to previous literature reports [39]. Raman spectra of graphite were collected at room temperature in back scattering geometry using an inVia Renishaw 1000 micro-Raman spectrometer equipped with 514 nm laser. Laser line was focused on the sample under a Leica DLML microscope.

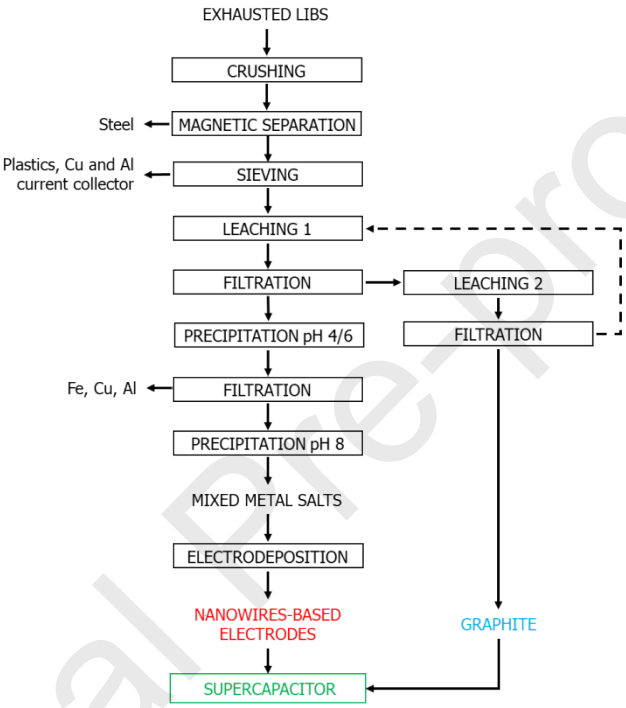

Fig. 1. Scheme of the proposed process.

3. Results and Discussion

After the mechanical treatment of the batteries a fraction mainly composed by Al and Cu current collectors, steel and plastics from casing and paper separators, was separated from the electrodic powder. Electrodic powder was leached following a consolidated route where a mixture of H_2SO_4 and H_2O_2 were employed [38] the attained extraction rates were reported in Tab.S1 of the Supporting Information File. The resulting suspension was filtered obtaining a carbonaceous solid and a metal bearing solution. The solution composition is reported in Table 1. As expected, cobalt was the most concentrated metal in the leaching solution, followed by Ni and Mn. $LiCoO_2$ was the most widespread cathode material employed in first LIBs generation and the currently collected end of life LIBs are still mainly represented by batteries containing $LiCoO_2$ [4,40]. The presence of a not negligible cadmium amount can be attributed to a contamination of collected end of life LIBs stock with Ni-Cd batteries. Al, Cu and Fe presence are imputed to the presence, in the electrodic powder, of batteries current collectors and casing with granulometry less than 0.5 mm. To evaluate the influence of the different metal impurities on the electrochemical behaviour of the positive nanowires-based electrode, selective precipitation of the leach liquor was separately conducted at pH 4 and 6. The metals contained in the leach liquors purified at pH 4 and 6 were subsequently precipitated as carbonates and used for the production of two electrolytic bath solutions Rec-4 and Rec-6, respectively. The liquid stream obtained after filtration is a Li-rich solution and could be employed for the recovery of lithium [41]. The baths composition obtained dissolving the two carbonates is reported in Tale 1. As compared to the leach liquor, Rec-4 and Rec-6 solutions were both purified from Fe and Al. In addition, copper concentration was 50 times lower in Rec-6 solution with respect to the original leach liquor. Figs. 2(a and b) display the SEM images of the nanowires-based electrode synthesized employing the produced solutions. Nanowires array with a thickness of about 4μm were obtained with both the employed solutions Rec-4 (Rec-4NW) and Rec-6 (Rec-6NW). The surface composition of the nanowire electrodes was extracted from XPS analysis.

Table 1. Composition [gL^{-1}] of the leach liquor and of the electrolytic baths obtained after the dissolution of the produced carbonates resulting from purification at pH 4 (Rec-4) and 6 (Rec-6).

Solution	Co	Ni	Mn	Cu	Fe	Cd	Al	Li
leach liquor	21.8	10.2	3.7	1.0	0.5	0.3	1.2	3.5
Rec-4	24.6	6.8	11.4	0.9	<5E-4	0.3	-	0.04
Rec-6	47.7	3.1	4.2	0.02	<5E-4	0.3	-	0.04

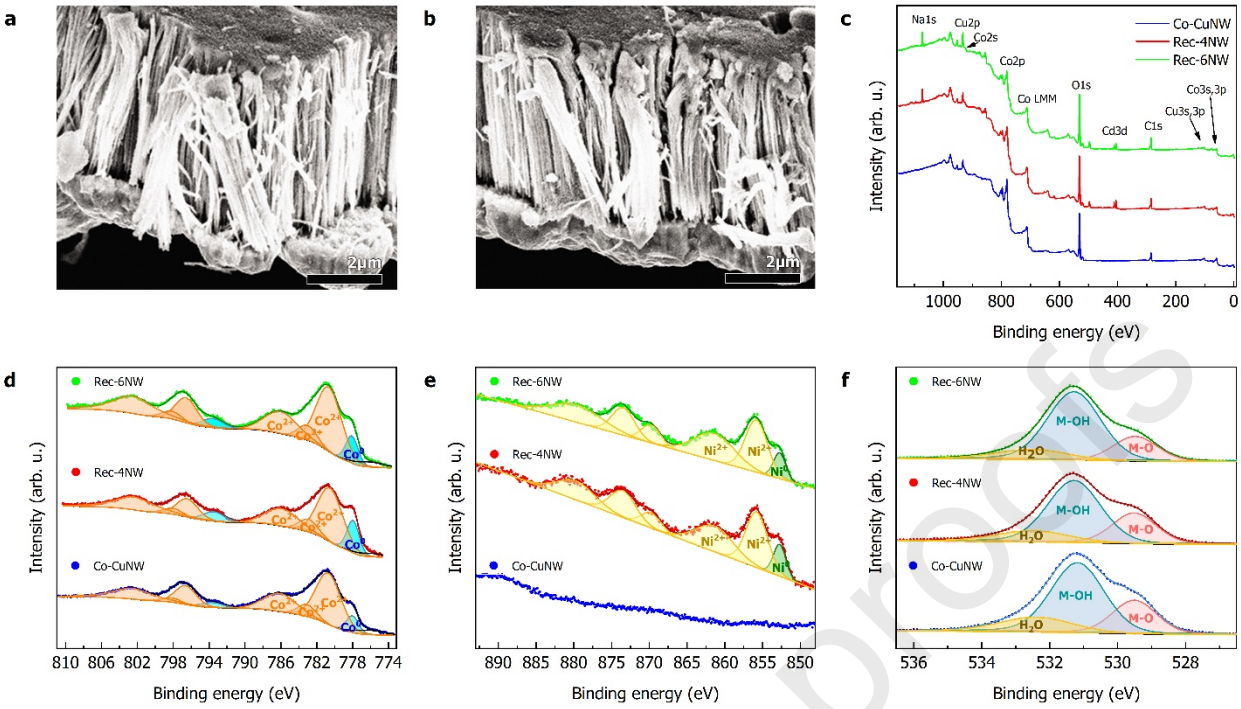

Fig. 2. SEM images of the nanowire electrodes Rec-4 (a) and Rec-6 (b). Wide range photoemission spectra of Co-Cu, Rec-4NW and Rec-6NW (c). Co 2*p* (d), Ni 2*p* (e), O 1*s* (f) XPS spectra.

Fig. 2(c) displays the XPS survey scans of the electrodes synthesized using the different electrolytic baths. The relative atomic ratios among main peaks are reported in Table 2. With the exception of the synthetic CoCuNW, the prevailing contributions to Rec-4NW and Rec-6NW can be attributed to Co (2*p*, 3*p* and 3*s*), Cu (2*p*, 3*p* and 3*s*) and Ni (2*p*) and Cd (3*d*). The simultaneous presence of Co and Cu hinders a straightforward identification of Mn through its most intense peak, Mn 2*p*, because its corresponding ionization region overlaps with the sequence of either Co LMM Auger excited by Mg Kα photons, or Cu L3M2,3M4,5 Auger lines, when Al Kα photons are employed. The intrinsic detectability limit in XPS is reported as 0.1% at the surface using Al and Mg Kα photons. By comparison with our laboratory test measurements, we can state that Mn, if present, is below 1 at%. This negligible percentage of Mn in the synthesized electrode can be explained by the larger cathodic potential required to attain the electrodeposition of Mn as compared to Cu, Co and Ni. Accordingly, at the potential that is applied during nanowire electrodeposition, the electrodeposition overpotential (i.e. difference between applied potential and the minimum cathodic potential required for electrodeposition), and thus the deposition rate, is significantly larger for Cu, Co and Ni than for Mn. In all the electrodes, Co and Ni present both metal and Me(II) oxide/hydroxide peak components, as revealed by curve fitting (Fig. 2d and e). Cu 2*p* peaks can be assigned to a combination of Cu(0) and (I) states, with no trace of Cu(II) component, as

Table 2. Electrodes composition (%) obtained from XPS analysis. $MeO+MeOH_2=CoO+Co(OH)_2+NiO+Ni(OH)_2$

Electrode	Cu	Co^0	$CoO+Co(OH)_2$	Ni^0	$NiO+Ni(OH)_2$	Cd	$MeO+MeOH_2$/Cu
Co-CuNW	8.1	8.1	83.8				10.3
Rec-4NW	13.1	10.7	58.1	1.9	10.2	6.0	5.2
Rec-6NW	6.4	7.8	60.7	2.5	18.0	4.6	12.3

can be inferred by close inspection of the Cu 2*p* and Cu LMM region in the wide spectra in Fig. 2(c) and by single spectra (not shown). The contemporary presence of metal and oxide peak components for the Ni, Co and Cu calls for a very thin oxidized surface layer in the nanometre scale. Cd is only present as Cd(II) oxide/hydroxide. Three components are extracted from each O 1*s* peak, which are respectively assigned, at increasing BE, to oxide, hydroxide and chemisorbed water. As can be inferred from Fig. 2(f), O 1*s* peaks reveal the large prevalence of metal hydroxides over oxides. A careful distinction between the two components for each metal cannot be confidently proposed. CoO and $Co(OH)_2$ present quite similar Co 2*p* spectra, and no clear-cut conclusion can be drawn about their relative presence in the samples. NiO and $Ni(OH)_2$ present distinct Ni 2*p* spectra, and, on the basis of the literature, the present assignment is to $Ni(OH)_2$ [42,43]. The nanowires electrodes were firstly tested in a three-electrode cell system to investigate their electrochemical behaviour. Fig. 3(a and b) display the cyclic voltammetry of the synthesized electrodes. To evaluate the role of the nickel in the nanowires structure, the results obtained using an electrode produced from a synthetic cobalt bath (CoNW) were also reported. The recorded voltammograms are characterized by the presence of evident peaks denoting that the capacitance is mainly determined by Faradaic contributions. The increase of peak currents of the CV redox peaks increased linearly with the square root of the scan rate (Fig. S1), confirming the battery-type charge storage mechanism of the nanowire-based electrodes [44,45]. The redox peaks in the CV curves can be attributed to the redox reaction between +2/+3 and +3/+4 oxidation states of Co and Ni as described by the following equations [25,46,47]:

$$MeO + OH^- \leftrightarrows MeOOH + e^- \quad (1)$$

$$Me(OH)_2 + OH^- \leftrightarrows MeOOH + H_2O + e^- \quad (2)$$

$$CoOOH + OH^- \leftrightarrows CoO_2 + H_2O + e^- \quad (3)$$

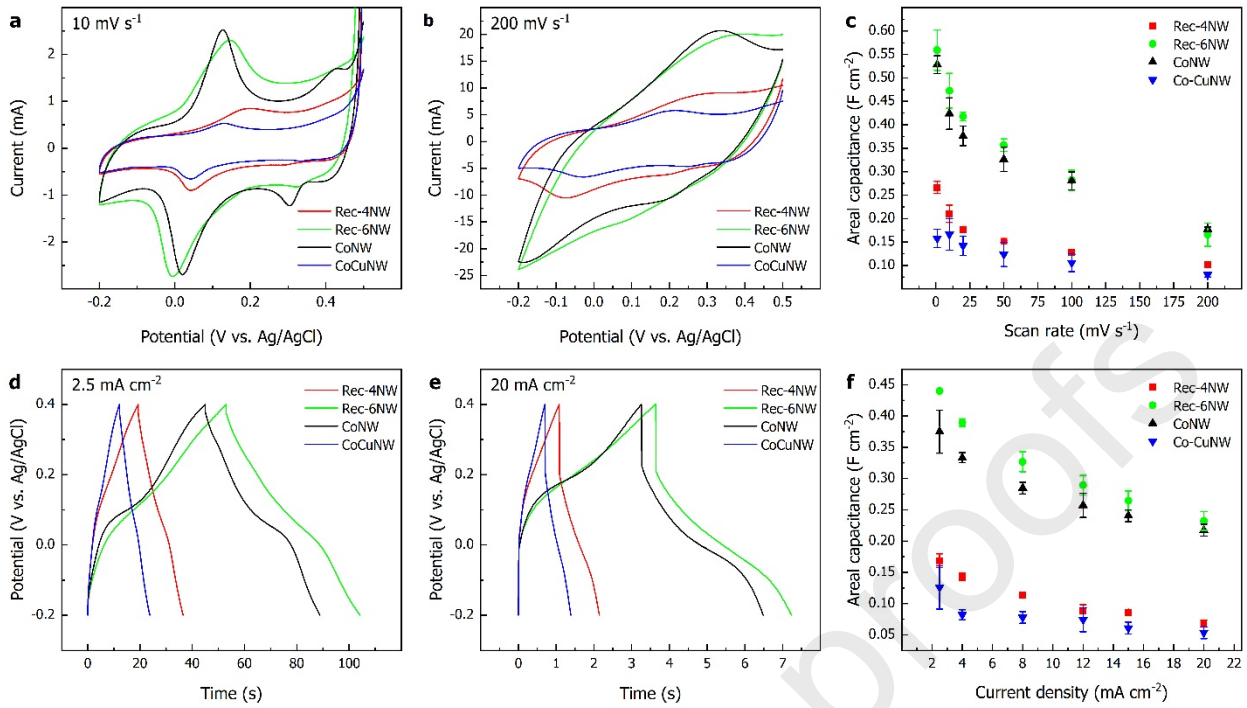

Fig. 3. Cyclic voltammograms (a) and charge-discharge curves recorded during galvanostatic cycling (b) of the electrodes CoNW, Co-CuNW, Rec-4NW and Rec-6NW. Areal capacitance values estimated from cyclic voltammetry (c) and galvanostatic cycling (d).

Where Me represents Co and Ni. The area under the recorded CV curves gives a first indication of the storage properties of any electrode and the areal capacitances computed using the CV areas (Eq.S1) were reported in Fig. 3(c). The electrochemical performance of nanowire-based electrodes was further investigated by galvanostatic cycling experiments, as shown in Fig. 3(d and e). For any electrode, a non-linear trend of the potential profile was found, and plateaus were found on the curves in a potential range according with cyclic voltammetry results. The occurrence of large plateaus is due to the above reported equation (Eq.1,2,3) and confirms the pseudocapacitance behaviour of the electrodes. The capacitance values computed (Eq.S2) from GC experiments were in good agreement with the CV results and, finally, highlighted the needed to perform the purification of leach liquor at the higher investigated pH value of 6 to remove copper impurity. In fact, the lower capacitance exhibited by CoCuNW can be attributed mainly to the copper content. As demonstrated by XPS analysis (Table 2), copper is mainly present in all the electrodes as metallic Cu with a minor part of Cu_2O and both these copper species are inactive along the investigated potential range [48,49]. The presence of Cu leads to a decrease in active materials loading hindering the charge storage and thus the final capacitance.

Rec-4NW electrode displays a MeO+$Me(OH)_2$/copper ratio (Me=Co, Ni) (Table 2) about half respect CoCuNW therefore, reasonably, its capacitance should be about half to respect CoCuNW. Remarkably, the capacitance shown by Rec-4NW is higher than CoCuNW. Furthermore, a difference can be noted between the capacitance of the Rec-6NW and CoNW. In this latter electrode, no copper was present and the active material $CoO/Co(OH)_2$ loading should be the highest. On the other hand, the capacitance values obtained for the Rec-6NW is higher than the synthetic CoNW electrode. The higher capacitances found in the recovered electrodes when benchmarked with the analogue synthetic electrodes can be attributed to the presence of $NiO/Ni(OH)_2$. As demonstrated in several works, compared to the unique cobalt or nickel oxides/hydroxides, cobalt-nickel oxides/hydroxides exhibit better electrochemical activity originating from the synergistic effect of nickel and cobalt which provide richer redox reactions, structure stability and electrical conductivity [25,46,50–53]. The carbonaceous solid resulting after leach liquor filtration is mainly composed of end of life LIBs anodic graphite material but, as shown in Tab.S2, the presence of metals requires a further leaching operation to purify the solid. Negligible metal contents were found after a second leaching performed under the same operating conditions of the first one (Tab.S2). It must be remarked here that, after filtration, the solution coming from the second leaching operation can be recycled to leach fresh electrodic powder in order to reduce reagent consumption and liquid wastes generation during the process. The recovered graphite (Rec-GPH) was chemically characterized in order to evaluate its possible reuse as negative electrodes in the asymmetric supercapacitor. Fig. 4 displays the characterization results of the Rec-GPH. SEM image (Fig. 4a) does not display the typical morphology of graphite where extremely close layers are present. Individual graphite nanosheets can be clearly observed and the presence of graphene consisting of several graphite sheets cannot be excluded [54]. The crystalline phase of the Rec-GPH was identified by XRD powder diffraction. XRD pattern of Rec-GPH is reported in Fig. 4(b) showing a sharp and tight peak, which corresponds to the diffraction line of C (002) in the typical crystal structure of graphite [55]. Fig. 4(c) illustrates the Raman spectra of the recovered graphite as compared with the spectra of pristine commercial graphite. The three Raman peaks that generally can be observed for graphene samples, indicated as G (1570 cm^{-1}), D (1360 cm^{-1}) and 2D peak (2720 cm^{-1}), are observed. The intensity ratio of I_D/I_G is used to characterize the order or disorder degree of carbon materials, i.e., the higher the I_D/I_G, the larger disorder degree of the carbon materials [56]. As can be seen, the Rec-GPH sample shows an intensity of the D peak higher (I_D/I_G=0.207) than the analogous peak

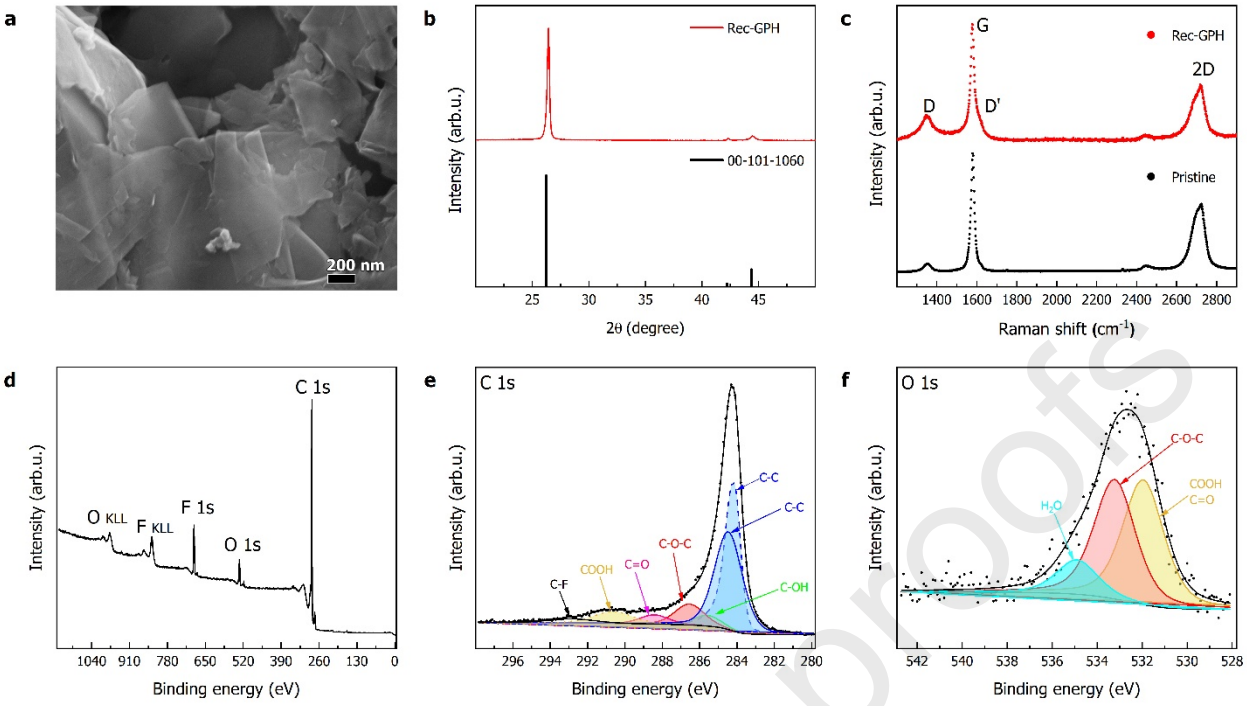

Fig. 4. (a) SEM image, (b) XRD and (c) Raman spectra of recovered graphite. (d) Wide range (e) C 1s and O 1s XPS spectra of the recovered graphite.

for pristine graphite (I_D/I_G=0.089). The D peak is related to defects density and is very low in pristine graphite. This higher I_D/I_G ratio could be a first indication of defects in Rec-GPH after the leaching treatment. Furthermore, the D' peak (1620 cm^{-1}), which comes from structural defects, was not found in pristine graphite [57]. On the other hand, the asymmetric shape of the 2D peak of Rec-GPH approaches that of graphite or a graphene with at least 10 graphite layers [58]. Further information on Rec-GPH comes from XPS measurements. Wide-range XPS spectrum of Rec-GPH discloses C, O and F as the major components (Fig. 4d). The presence of fluorine can be due to residues of polyvinylidene fluoride (PVDF), employed as a binder during the batteries assembly, as confirmed by the C-F components found on the C 1*s* spectrum (Fig. 4e). XPS relative quantitative measurements show oxygen and carbon contents respectively of 6.5% and 93.5%, with a C/O ratio of 14.4, a value close to literature reports from XPS measurements of reduced graphene oxide (rGO) [59]. As recently demonstrated [60], graphite anode undergoes several lithiation and de-lithiation processes during batteries cycling, enabling pre-expansion of graphite layers. Furthermore, a recent work [60] demonstrates that the acid leaching performed to dissolve the cathodic materials during the recovery of

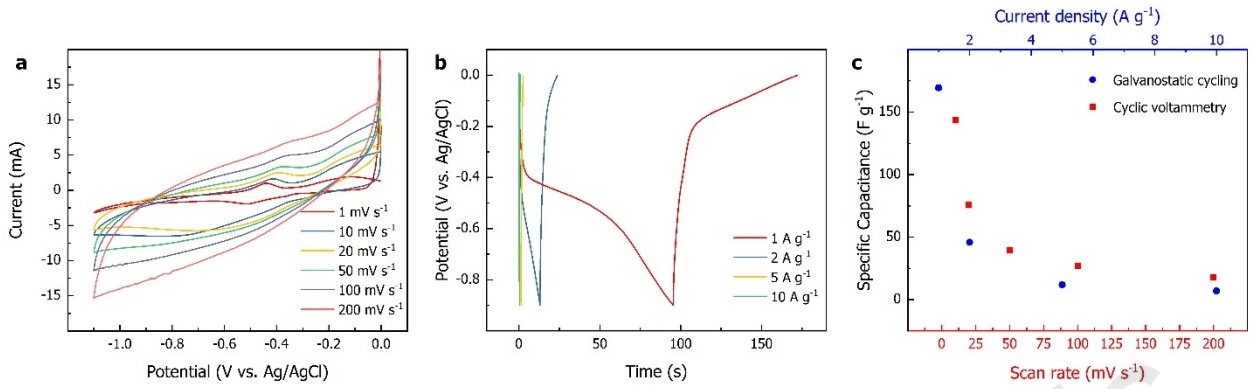

Fig. 5. Cyclic voltammograms (a) and charge-discharge curves recorded during galvanostatic cycling (b) of the recovered. Specific capacitance values estimated from cyclic voltammetry and galvanostatic cycling (c).

graphite from end of life LIBs, further swells the graphite lattice, increasing the graphene productivity by a factor of 10 with respect to pristine graphite. This result can be justified by considering the introduction of several functional groups after the acidic treatment of the graphite, which prevents aggregation of graphene flakes. The C 1*s* and O 1*s* XPS spectra (Fig. 4e and f) indicate the occurrence of C-OH (~285 eV), C-O (~286 eV), C=O (~289 eV) and COOH (~290 eV) functional groups. The similarity in C/O ratio between Rec-GPH and rGO hints at the obtainment of a partial exfoliation of the graphite recovered using the proposed process. Rec-GPH was tested in the three-electrode cell configuration to evaluate its electrochemical behaviour as negative electrode in the asymmetric capacitor. Fig. 5(a) shows the cyclic voltammograms of Rec-GPH at various scan rates. It is well known as carbon materials shows rectangular curve shape without observation of redox peaks, and the charge storage involves typical non-faradic adsorption/desorption reactions [61]. On the other hand, cathodic/anodic shoulders can be seen at about -0.4 V and are related to the redox reactions of oxygenated functionalities discovered by the XPS analysis [62–64]. The galvanostatic cycling experiments (Fig.5b) confirm the capacity trend value obtained from the CV and plateaus were observed in same potential values. Remarkably, capacitances obtained by CV and GC are comparable to the best values reported for graphene-based supercapacitors [65–67]. In addition, a comparison between Rec-GPH and new battery grade graphite (TIMREX KS6) was performed. As shown in Fig.S2, Rec-GPH has specific capacitance values close to KS6 graphite when the specific capacitance was computed from CV scans. On the other hand, a significative higher capacitance (~ 220 vs. 170 F g^{-1}) was found for the KS6 graphite using galvanostatic charge-discharge curves for the estimation of the capacitance. This result could be explained by the difference on the BET surface area of the Rec-GPH and KS6 graphite. In fact, after BET measurement (Fig. S3) we found a BET

surface area of 4.6 ± 0.5 m^2 g^{-1} for the recovered graphite while the declared BET surface area of the KS6 graphite is 26 m^2 g^{-1}. The CV scans of nanowires-based and graphite electrodes, recorded using three-electrode system, were employed to evaluate the stability potential window when the electrodes were assembled in a two-electrode supercapacitor. According to the cyclic voltammograms reported in Fig. 6(a), a potential window of 1.5 V was selected for the testing of the electrochemical device. For the supercapacitor assembly (Fig.S4), the charge storage balance between the two electrodes was reached tuning the mass loading of the Rec-GPH negative electrode using the Eq.S3. Galvanostatic cycling experiments were carried out at 2.5 mA cm^{-2} and the results for all the fabricated supercapacitors were reported in Fig. 6(b). Charge-discharge curves reveal as the supercapacitor assembled using the Rec-6NW positive electrode was characterized by the higher discharge duration, i.e. capacitance. Durability of the as-fabricated asymmetric supercapacitors were tested cycling the device until 2000 cycles. Capacitance values recorded during cycling were reported in Fig. 6(c). Rec-6NW//Rec-GPH fully recycled supercapacitor shows the higher starting capacitance values of 42 Fg^{-1}. Quite similar capacitance values (30 Fg^{-1}) were found between Rec-4NW and

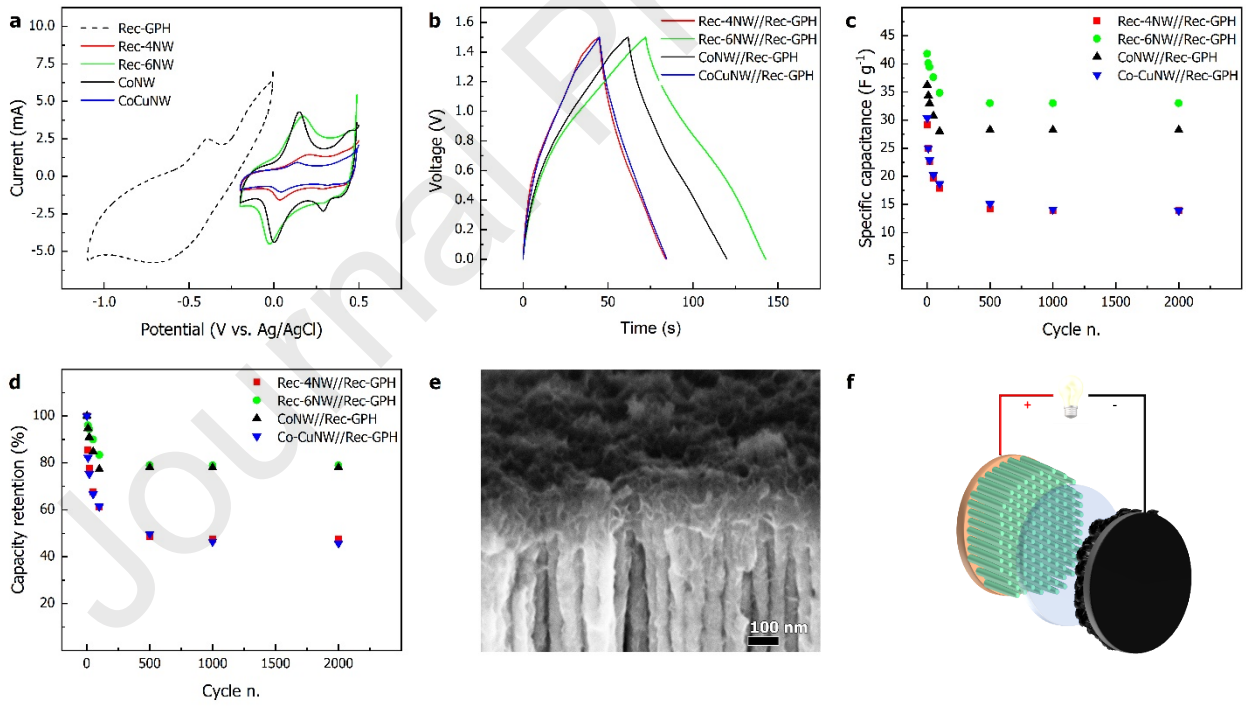

Fig. 6. (a) Cyclic voltammograms showing the potential stability window of the electrodes. (b) Galvanostatic charge-discharge curves of the asymmetric supercapacitors at 2.5 mA cm-2 (~0.5 A g-1 respect graphite). (c) Specific capacitance values estimated from galvanostatic cycling using the whole weight of the electrode (including current collector). (d) Cyclic performance of the asymmetric supercapacitor in the voltage window between 0 to 1.5 V. (e) SEM image of the Rec6-NW after galvanostatic cycling. (f) Schematic of the assembled asymmetric supercapacitor.

CoCuNW based supercapacitors, confirming the negative effect of the copper content on the produced electrodes. It must be noted that the masses used in the specific capacitances calculation were the sum of the nanowires-based electrodes, including current collector, and the graphite weights. Capacitance retention along the cycling was reported in Fig. 6(d). A sharp decrease in the capacitance values were found in all the supercapacitors in the first 100 cycles. Rec-6NW and CoNW supercapacitors retain about 80% of their initial capacitance after 100 cycles and the capacitance retention remain almost constant until 2000 cycles. A great loss on capacitance was found in the Rec-4NW and CoCuNW based supercapacitors with capacitance values lower than 50% respect their initial values. A flakes film was found on Rec-6NW positive electrodes surface after its cycling (Fig. 6e). The same flakes film was found in all the produced nanowires electrodes after galvanostatic cycling. Flakes are almost invariably formed as the result of Co and/or Ni hydroxide precipitation. It is thus likely that the flakes film formed over nanowires during cycling could be related to the formation and conversion of Ni and Co hydroxides. Particularly, the conversion of $Me(OH)_2$ to MeOOH (Me=Ni, Co) during charging, and vice versa during discharging, can induce a change in the morphology of the $Me(OH)_2$ thin layer that initially cover the nanowires. In addition, a partial dissolution of metallic Me that compose the core of the nanowires to Me2+ could occur. Precipitation of Me^{2+} as $Me(OH)_2$ on the surface of the electrode allowed by KOH electrolyte cannot be excluded. The formation of this layer probably hinders the diffusion of reactants through the nanowires array decreasing the recorded capacitance. Performances of any energy storage devices can be described by their energy and power density. Obtained results for any assembled supercapacitor thus were displayed in the Ragone's plot (Fig. S5). Rec-6NW//Rec-GPH supercapacitor yields a maximum energy density of ~9 Wh kg^{-1} and a power density of 416 W kg^{-1} at 2.5 mA cm^{-2}. These latter crucial parameters and the recorded capacitance are close to the best values of asymmetric supercapacitor based on carbonaceous negative electrode and Co-Ni metal based positive electrodes (Tab.S3) [9,68–70].

4. Conclusions

A new recycling process was proposed to directly produce asymmetric supercapacitors from spent LIBs. The process allows recovering the graphite and the cathode metals (Co and Ni) from the electrode powder of spent LIBs. The supercapacitor positive electrode was fabricated by template nanowire electrodeposition from electrolytic solutions prepared using the metals recovered from the LIB electrode powder. The role of copper

impurities was evaluated by the purification of the leach liquor at different pH values, while the effect of nickel in the nanowires electrodes was estimated by benchmarking the electrodes produced from spent LIBs with the electrodes produced using a synthetic cobalt solution. The presence of inactive copper in the nanowires lowered the final capacitance of the electrodes, while nickel showed a synergistic effect with cobalt providing a higher capacitance with respect to synthetic cobalt electrodes. The carbonaceous solid recovered after leaching was employed in the supercapacitor as the negative electrode material. Both the chemical and electrochemical analyses indicate that the recovered graphite is characterized by the presence of oxygen functionalities introduced by the leaching treatment. This gave a graphite with XPS C/O ratio, Raman spectrum and morphology close to those previously reported for reduced graphene oxide. The asymmetric supercapacitor assembled using the recovered nanowires-based positive electrodes and the graphite as negative electrodes showed electrochemical performances close to the best values reported for Co-Ni and graphene based supercapacitors. The illustrated study demonstrates that both the metals and carbon fractions from the electrode powder of spent LIBs can be simultaneously recovered and employed to directly produce high performance nanostructured electrode materials for supercapacitors. This result is achieved with the proposed recycling process by discarding the need to separate the electrode metals into high purity streams, which is a costly and complex operation performed today by traditional hydrometallurgical and pyrometallurgical processes. By eliminating the numerous stages (solvent extraction and stripping stages, numerous precipitations, electrowinning) that are today performed to separate the electrode metals, a significant reduction in the capital and operating expenditures can be attained along with a reduction of the environmental footprint.

References

[1] F. Arshad, L. Li, K. Amin, E. Fan, N. Manurkar, A. Ahmad, J. Yang, F. Wu, R. Chen, ACS Sustainable Chemistry & Engineering, 8 (2020) 13527-13554.
[2] R.E. Ciez, J.F. Whitacre, Nature Sustainability, 2 (2019) 148-156.
[3] J. Arambarri, J. Hayden, M. Elkurdy, B. Meyers, Z.S.A. Hamatteh, B. Abbassi, W. Omar, Environmental Engineering Research, 24 (2019) 699-710.
[4] H. Zou, E. Gratz, D. Apelian, Y. Wang, Green Chemistry, 15 (2013) 1183-1191.

[5] W. Chu, Y. Zhang, X. Chen, Y. Huang, H. Cui, M. Wang, J. Wang, J. Power Sources, 449 (2020) 227567.
[6] S. Natarajan, K. Subramani, Y.-S. Lee, M. Sathish, V. Aravindan, J. Alloys Compd., 827 (2020) 154336.
[7] S. Natarajan, V. Aravindan, Advanced Energy Materials, n/a (2020) 2002238.
[8] S. Natarajan, V. Aravindan, Advanced Energy Materials, 8 (2018) 1802303.
[9] Y.I. Mesbah, N. Ahmed, B.A. Ali, N.K. Allam, 7 (2020) 975-982.
[10] J. Wu, A. Mackenzie, N. Sharma, Green Chemistry, 22 (2020) 2244-2254.
[11] T. Or, S.W.D. Gourley, K. Kaliyappan, A. Yu, Z. Chen, 2 (2020) 6-43.
[12] M.L. Divya, S. Natarajan, Y.-S. Lee, V. Aravindan, ChemSusChem, n/a (2020).
[13] V. Aravindan, S. Jayaraman, F. Tedjar, S. Madhavi, 6 (2019) 1407-1412.
[14] S. Natarajan, M. Ulaganathan, H.C. Bajaj, V. Aravindan, ChemElectroChem, 6 (2019) 5283-5292.
[15] K.-C. Ho, L.-Y. Lin, Journal of materials chemistry A, 7 (2019) 3516-3530.
[16] E. Mourad, L. Coustan, P. Lannelongue, D. Zigah, A. Mehdi, A. Vioux, S.A. Freunberger, F. Favier, O. Fontaine, Nature materials, 16 (2017) 446-453.
[17] K. Krishnamoorthy, P. Pazhamalai, S. Sahoo, J.H. Lim, K.H. Choi, S.J. Kim, 4 (2017) 3302-3308.
[18] K.-J. Huang, J.-Z. Zhang, J.-L. Cai, Electrochim. Acta, 180 (2015) 770-777.
[19] C. Xiong, T. Li, A. Dang, T. Zhao, H. Li, H. Lv, J. Power Sources, 306 (2016) 602-610.
[20] B. Li, M. Zheng, H. Xue, H. Pang, Inorganic Chemistry Frontiers, 3 (2016) 175-202.
[21] Q. Li, S. Zheng, Y. Xu, H. Xue, H. Pang, Chem. Eng. J., 333 (2018) 505-518.
[22] S. Korkmaz, F.M. Tezel, İ. Kariper, J. Alloys Compd., 754 (2018) 14-25.
[23] X. Zhou, H. Dai, X. Huang, Y. Ren, Q. Wang, W. Wang, W. Huang, X. Dong, Materials Today Energy, 17 (2020).
[24] H. Xu, Y. Cao, Y. Li, P. Cao, D. Liu, Y. Zhang, Q. Li, Journal of Energy Chemistry, 50 (2020) 240-247.
[25] H.C. Chen, Y. Qin, H. Cao, X. Song, C. Huang, H. Feng, X.S. Zhao, Energy Storage Materials, 17 (2019) 194-203.
[26] M. Li, K.Y. Ma, J.P. Cheng, D. Lv, X.B. Zhang, J. Power Sources, 286 (2015) 438-444.
[27] T.N.J.I. Edison, R. Atchudan, Y.R. Lee, Electrochim. Acta, 283 (2018) 1609-1617.
[28] J. Zhao, Y. Tian, A. Liu, L. Song, Z. Zhao, Mater. Sci. Semicond. Process., 96 (2019) 78-90.
[29] H. Xu, Y. Cao, Y. Li, P. Cao, D. Liu, Y. Zhang, Q. Li, Journal of Energy Chemistry, (2020).
[30] S. Ghosh, P. Samanta, N.C. Murmu, T. Kuila, J. Alloys Compd., (2020) 155432.
[31] M. Li, A. Addad, M. Dolci, P. Roussel, M. Naushad, S. Szunerits, R. Boukherroub, Chem. Eng. J., (2020) 125370.
[32] L. Zhang, D. Shi, T. Liu, M. Jaroniec, J.J.M.T. Yu, 25 (2019) 35-65.
[33] L. Wang, H. Wang, C. Qing, G. Qu, W. Ma, Y. Tang, J. Alloys Compd., 726 (2017) 139-147.
[34] P.G. Schiavi, L. Farina, R. Zanoni, P. Altimari, I. Cojocariu, A. Rubino, M.A. Navarra, S. Panero, F. Pagnanelli, Electrochim. Acta, 319 (2019) 481-489.
[35] P.G. Schiavi, L. Farina, P. Altimari, M.A. Navarra, R. Zanoni, S. Panero, F. Pagnanelli, Electrochim. Acta, 290 (2018) 347-355.
[36] E.A.A. Aboelazm, G.A.M. Ali, H. Algarni, H. Yin, Y.L. Zhong, K.F. Chong, The Journal of Physical Chemistry C, 122 (2018) 12200-12206.
[37] A.K.S. Rocha, L.B. Magnago, J.J. Santos, V.M. Leal, A.A.L. Marins, V.C.B. Pegoretti, S.A.D. Ferreira, M.F.F. Lelis, M.B.J.G. Freitas, Mater. Res. Bull., 113 (2019) 231-240.
[38] F. Pagnanelli, E. Moscardini, P. Altimari, T. Abo Atia, L. Toro, Waste Manage. (Oxford), 60 (2017) 706-715.
[39] M.P. Seah, D. Briggs, Practical Surface Analysis: Auger and X-ray Photoelectron Spectroscopy, John Wiley & Sons, 1990.
[40] E. Gratz, Q. Sa, D. Apelian, Y. Wang, J. Power Sources, 262 (2014) 255-262.
[41] M. Chen, Z. Zheng, Q. Wang, Y. Zhang, X. Ma, C. Shen, D. Xu, J. Liu, Y. Liu, P. Gionet, Scientific reports, 9 (2019) 1654.
[42] M.C. Biesinger, B.P. Payne, L.W.M. Lau, A. Gerson, R.S.C. Smart, Surface and Interface Analysis: An International Journal devoted to the development and application of techniques for the analysis of surfaces, interfaces and thin films, 41 (2009) 324-332.

[43] M.C. Biesinger, B.P. Payne, A.P. Grosvenor, L.W. Lau, A.R. Gerson, R.S.C. Smart, Appl. Surf. Sci., 257 (2011) 2717-2730.
[44] P. Simon, Y. Gogotsi, B. Dunn, Science, 343 (2014) 1210-1211.
[45] T. Brousse, D. Bélanger, J.W. Long, J. Electrochem. Soc., 162 (2015) A5185-A5189.
[46] C.-M. Wu, C.-Y. Fan, I.W. Sun, W.-T. Tsai, J.-K. Chang, J. Power Sources, 196 (2011) 7828-7834.
[47] M. Wei, Q. Huang, Y. Zhou, Z. Peng, W. Chu, Journal of Energy Chemistry, 27 (2018) 591-599.
[48] S.K. Shinde, D.P. Dubal, G.S. Ghodake, V.J. Fulari, RSC Advances, 5 (2015) 4443-4447.
[49] J.L. Yin, J.Y. Park, Microporous Mesoporous Mater., 200 (2014) 61-67.
[50] C. Wang, P. Sun, G. Qu, J. Yin, X. Xu, Chin. Chem. Lett., 29 (2018) 1731-1740.
[51] L. Huang, D. Chen, Y. Ding, S. Feng, Z.L. Wang, M. Liu, Nano Lett., 13 (2013) 3135-3139.
[52] J. Yang, C. Yu, C. Hu, M. Wang, S. Li, H. Huang, K. Bustillo, X. Han, C. Zhao, W. Guo, Z. Zeng, H. Zheng, J. Qiu, Adv. Funct. Mater., 28 (2018) 1803272.
[53] C. Wang, E. Zhou, W. He, X. Deng, J. Huang, M. Ding, X. Wei, X. Liu, X. Xu, Nanomaterials, 7 (2017) 41.
[54] C. Tan, X. Cao, X.-J. Wu, Q. He, J. Yang, X. Zhang, J. Chen, W. Zhao, S. Han, G.-H.J.C.r. Nam, 117 (2017) 6225-6331.
[55] L.M. Rivera, S. Fajardo, M.D.C. Arévalo, G. García, E. Pastor, Catalysts, 7 (2017) 278.
[56] L.G. Cançado, A. Jorio, E.H.M. Ferreira, F. Stavale, C.A. Achete, R.B. Capaz, M.V.d.O. Moutinho, A. Lombardo, T.S. Kulmala, A.C. Ferrari, Nano Lett., 11 (2011) 3190-3196.
[57] Y. Zhang, B. Cao, B. Zhang, X. Qi, C. Pan, Thin Solid Films, 520 (2012) 6850-6855.
[58] S. Roscher, R. Hoffmann, O. Ambacher, Analytical Methods, 11 (2019) 1224-1228.
[59] P. Wick, A.E. Louw‐Gaume, M. Kucki, H.F. Krug, K. Kostarelos, B. Fadeel, K.A. Dawson, A. Salvati, E. Vázquez, L. Ballerini, Angew. Chem. Int. Ed., 53 (2014) 7714-7718.
[60] Y. Zhang, N. Song, J. He, R. Chen, X. Li, Nano Lett., 19 (2019) 512-519.
[61] H.-Q. Li, Y.-G. Wang, C.-X. Wang, Y.-Y. Xia, J. Power Sources, 185 (2008) 1557-1562.
[62] M.P. Bichat, E. Raymundo-Piñero, F. Béguin, Carbon, 48 (2010) 4351-4361.
[63] S. Shivakumara, B. Kishore, T.R. Penki, N. Munichandraiah, Solid State Commun., 199 (2014) 26-32.
[64] Y.J. Oh, J.J. Yoo, Y.I. Kim, J.K. Yoon, H.N. Yoon, J.-H. Kim, S.B. Park, Electrochim. Acta, 116 (2014) 118-128.
[65] A. Kumar, N. Kumar, Y. Sharma, J. Leu, T.Y. Tseng, Nanoscale Research Letters, 14 (2019) 266.
[66] J. Lyu, M. Mayyas, O. Salim, H. Zhu, D. Chu, R.K. Joshi, Materials Today Energy, 13 (2019) 277-284.
[67] H. Wang, Y. Song, W. Liu, L. Yan, J. Alloys Compd., 735 (2018) 2428-2435.
[68] C. Fang, D. Zhang, Journal of Materials Chemistry A, (2020).
[69] L. Liu, A. Liu, Y. Xu, H. Yu, F. Yang, J. Wang, Z. Zeng, S. Deng, J. Mater. Res., 35 (2020) 1205-1213.
[70] K. Yan, J. Wu, Y.-Y. Wang, N.-N. Liu, J.-T. Li, Y.-P. Gao, Z.-Q. Hou, Chemical Papers, 74 (2020) 591-599.

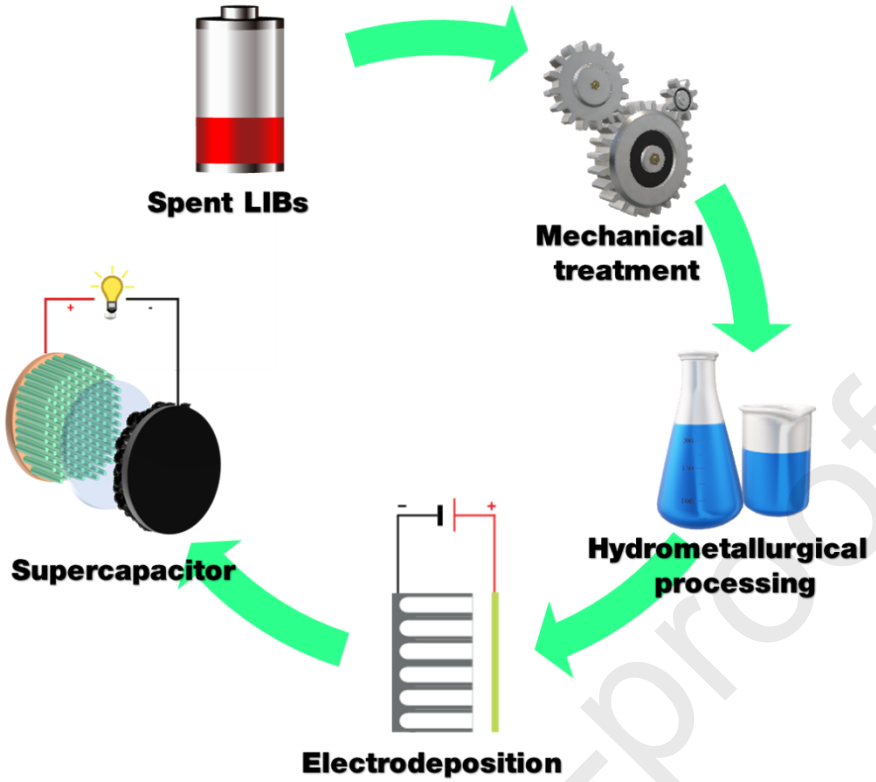

Graphical Abstract: Electrodic powder coming from real waste spent lithium ion batteries was employed as raw material for the production of asymmetric supercapacitor allowing the full recycling of the electrodic powder components

Declaration of interests

☒ The authors declare that they have no known competing financial interests or personal relationships that could have appeared to influence the work reported in this paper.

☐The authors declare the following financial interests/personal relationships which may be considered as potential competing interests: